Journal of Engineering and Applied Sciences 13 (21): 8955-8965, 2018
ISSN: 1816-949X

Effects of Aerodynamic Appendices on the Flutter Characteristics of Long-span Bridge Decks

G. Cannata, L. Barsi and F. Gallerano
Department of Civil, Construction and Environmental Engineering,
Sapienza University of Rome via. Eudossiana 18, 00184 Rome, Italy

Abstract: This research deals with the effects produced by aerodynamic appendices on the aeroelastic stability of long-span bridge decks. A simulation model is presented by which the structural motion and the fluid flow are together and simultaneously simulated. The deck is schematised as a bidimensional two-degree-of-freedom rigid oscillator, whilst the aerodynamic fields are simulated by numerically solving the 2D Arbitrary Lagrangian-Eulerian (ALE) formulated Unsteady Reynolds-Averaged Navier-Stokes (URANS) equations on moving meshes which adjust to the deck motion. The proposed finite volume method is based on high order Weighted Essentially Non-Oscillatory (WENO) reconstructions. The time discretisation is performed by a five stage fourth order accurate Strong Stability Preserving Runge-Kutta (SSPRK) method. It is shown that the proposed numerical method makes it possible to ensure both high accuracy in time and space. The simulation model is validated by comparing the numerical results with experimental data and is applied to the evaluation of the aeroelastic stability of the forth road suspension bridge deck. The effects of aerodynamic appendices on the flutter characteristics of the forth road bridge are investigated via the proposed simulation model. It is demonstrated that the presence of the cross-section details (barriers, railings, dividing strips) makes the aeroelastic stability of the deck worse and that the flutter sensitivity is mitigated by introducing a couple of sloping barriers at the edges of the deck.

Key words: Turbulence model, moving meshes, finite volume, bridge flutter, aerodynamic fields, effects

INTRODUCTION

Long span bridges are susceptible to an oscillatory unstable aero-elastic phenomenon, named flutter, in which the bridge deck motion acquires a divergent character and the oscillation amplitudes grow rapidly to the point of causing the structural failure (Dowell, 2014). Bridge decks with bluff cross-sections are generally prone to the torsional flutter phenomenon: the case of the Tacoma Narrows Bridge deck is a well known example. Larsen (2000) highlight that the torsional flutter phenomenon is related to the formation and the drift of large vortices along the surface of the structure as it undergoes a change in the angle of attack. Bridge decks with streamlined cross-sections are generally prone to the coupled (torsional-flexural) flutter phenomenon: the possibility that the latter kind of instability takes place is relevant in the case in which the bridge deck has torsional and flexural natural modes of oscillation closely spaced at low natural frequencies (Frandsen, 2004). Matsumoto *et al*. (2010) carried out extensive analytical investigations on the mechanisms of coupled flutter. These researchers distinguish two different types of coupled flutter. The first type is the Torsional Branch (TB) coupled flutter which is dominated by a fundamentally torsional vibration and in which the vertical oscillations have small amplitudes. The second type is the Heaving-Branch (HB) coupled flutter which is dominated by a fundamentally heaving vibration accompanied by torsional oscillations with small amplitudes.

Traditionally the critical flutter wind velocity of long span bridge decks is identified through the Scanlan approach (Scanlan and Tomko, 1971). A central element of the Scanlan approach lies in modelling the aerodynamic forces as linear functions of the structural displacements, under the assumption of purely sinusoidal motions. This linear dependence is expressed via., some appropriate coefficients, called flutter derivatives which are usually identified through the so-called forced oscillation method. Astiz (1998) and Dowell (2014) highlight that the above linear relation proves to be acceptable only in the event that the amplitude of structural oscillations is limited. Furthermore, the latter researcher highlight that the same linear relation does not make it possible to take into

Corresponding Author: G. Cannata, Department of Civil, Construction and Environmental Engineering,
Sapienza University of Rome via. Eudossiana 18, 00184 Rome, Italy

account the effects of the unsteady vortical formations which can be developed in the fluid-structure interaction. An alternative approach, followed by different researchers, Robertson *et al*. (2003), Frandsen (2004) Braun and Awruch (2008) consists in simulating the aerodynamic fields and the structural motion simultaneously and in a coupled manner so as to allow the identification of the critical flutter wind velocity in a direct way. In the models proposed by the above-mentioned research the structure is represented as a bidimensional rigid body with two degrees of freedom, having mass per unit length and mass moment of inertia per unit length equal to those of the deck.

Many research simulate the fluid dynamic fields with finite volume techniques on unstructured grids (Oka and Ishihara, 2009; Bruno and Khris, 2003; Cioffi and Gallerano, 2006) and on structured grids (Cheng *et al*., 2003; Gallerano and Cannata, 2011a, b; Haque *et al*., 2016; Gallerano *et al*., 2016a, b). In the case in which the simulations of the fluid dynamic fields involve moving boundaries, the fluid motion equations have to be formulated according to the Arbitrary Lagrangian-Eulerian Approach (ALE) (Zhu *et al*., 2007; Miranda *et al*., 2014; Nieto *et al*., 2015).

In this research, a simulation model is presented by which the structural motion and the fluid flow are together and simultaneously simulated. The deck is schematised as a bidimensional two-degree-of-freedom rigid oscillator, whilst the aerodynamic fields are simulated by numerically solving the Arbitrary Lagrangian-Eulerian (ALE) formulated 2D Unsteady Reynolds-Averaged Navier-Stokes (URANS) equations on moving meshes which adjust to the deck motion. The proposed finite volume method is based on high order Weighted Essentially Non-Oscillatory (WENO) reconstructions. The time discretisation is performed by a five stage fourth order accurate Strong Stability Preserving Runge-Kutta (SSPRK) method. The accuracy of the proposed numerical method is checked by conducting the grid convergence test proposed by Roache (1998) in static conditions (i.e., all the degrees of freedom of the cross-section are restrained): the time averaged and the root-mean-square values of the drag coefficient, the lift coefficient and the moment coefficient, together with the value of the Strouhal number are taken as parameter of interest. The model validation is performed in dynamic conditions (i.e., the cross-section is free to oscillate in the bending degree of freedom and in the torsional degree of freedom) by comparing the numerical results with the experimental data reported by Robertson *et al*. (2003): this comparison is performed in terms of critical flutter wind velocity and root mean square of rotational displacements.

A deep insight into the analysis and the detailed representation of the different phenomena that produce the onset and the amplification of the flutter instability for long span bridge decks is proposed. The effects of aerodynamic appendices on the flutter characteristics of the forth road bridge are investigated via the proposed simulation model. It is demonstrated that the presence of the cross-section details (barriers, railings, dividing strips) makes the aeroelastic stability of the deck worse and that the flutter sensitivity is mitigated by introducing a couple of sloping barriers at the edges of the deck.

MATERIALS AND METHODS

The governing equations of fluid flow: The ALE formulated ensemble averaged continuity and momentum equations in integral form read as follows (Hertel *et al*., 2013):

$$\frac{d}{dt}\int_{\Delta A} dA + \int_{L}\left[\langle u_i\rangle - u_{g,i}\right]n_i\,dL = 0 \tag{1}$$

$$\frac{d}{dt}\int_{\Delta A}\langle u_i\rangle dA = -\int_{L}\langle u_i\rangle\left[\langle u_j\rangle - u_{g,j}\right]n_j dL + \int_{\Delta A}\frac{\partial}{\partial x_j}\left[2\nu\langle S_{ij}\rangle - \langle u_i' u_j'\rangle\right]dA + \int_{\Delta A} f_i\,dA - \int_{\Delta A}\frac{\partial\langle P\rangle}{\partial x_i}dA \tag{2}$$

Where:

- dA = The Area of a surface element whose contour line is L
- n_j = The outward normal
- u_i and P = The ensemble-averaged i-th component of the fluid velocity and the ensemble-averaged fluid pressure
- $u_{g\,I}$ = The i-th component of the grid velocity
- ν = The kinematic viscosity
- f_i = The component of the mass force vector

The unknown term $\langle u_i' u_j'\rangle$ which can be defined as the Reynolds tensor is related to the ensemble averaged strain rate tensor $\langle S_{ij}\rangle$ and the ensemble averaged turbulent kinetic energy per unit mass $\langle k\rangle$ through the relation:

$$\langle u_i' u_j'\rangle = -2\nu_t\langle S_{ij}\rangle + \frac{2}{3}\langle k\rangle\delta_{ij} \tag{3}$$

Where:

- ν_t = The kinematic Eddy viscosity
- δ_{ij} = The Kronecker symbol

The turbulent closure relations for the ensemble-averaged motion equations can be expressed as a function of the turbulent kinetic energy k and the rate of

viscous dissipation ϵ or as a function of the turbulent kinetic energy and the turbulence frequency ω. Menter (2009) proposed the k-ω Shear Stress Transport (SST) model which consists of a blending between the k-ϵ and k-ω models. In this research the turbulence closure relations and the calibration parameters which are included in them are derived from (Menter, 2009).

The governing equations of structural motion: The governing equations of the bidimensional elastically suspended rigid body with two degrees of freedom read as follows (Li *et al*., 2002):

$$m\ddot{\eta} + S\ddot{\theta} + c_y\dot{\eta} + k_y\eta = f_y(\eta,\dot{\eta},\ddot{\eta},\theta,\dot{\theta},\ddot{\theta}) \quad (4)$$

$$I\ddot{\theta} + S\ddot{\eta} + c_\theta\dot{\theta} + k_\theta\theta = m_\theta(\eta,\dot{\eta},\ddot{\eta},\theta,\dot{\theta},\ddot{\theta}) \quad (5)$$

where, m and I are respectively, the mass and the mass moment of inertia per unit length of the deck, S is the static imbalance equal to m times the distance a between the shear centre and the centre of mass, c_y and c_θ are respectively, the structural damping coefficients in the vertical and torsional degree of freedom, k_y and k_θ are respectively, the stiffness constant of the vertical elastic spring and the stiffness constant of the torsional elastic spring, f_y and m_θ are respectively, the component in the y direction of the force exerted by the aerodynamic field on the body and the twisting moment generated by the above-mentioned force on the body and η and θ are respectively, the vertical displacement of the centre of gravity of the body and the rotational angle of the body around the shear centre. The stiffness k_y and k_θ are calibrated in order to give the natural frequencies corresponding to the fundamental flexural and torsional natural modes of vibration of the structure. The damping coefficients are calculated according to the hypothesis of classical viscous damping on the basis of the given damping ratios. The components f_y and the twisting moment m_θ are calculated by integrating the pressures, the viscous stresses and the turbulent stresses over the surface of the structure. The structural motion equations are solved by a second-order accurate scheme and the coupling between the fluid solver and the structure solver follows a partitioned loose-coupling approach (Li *at al*., 2002).

The numerical scheme: Let us define $\langle\bar{u}_i\rangle$ and $\langle\bar{P}\rangle$ as the cell averaged values of the velocity vector and the pressure:

$$\langle\bar{u}_i\rangle = \frac{1}{\Delta A}\int_{\Delta A}\langle u_i\rangle dA,\ \langle\bar{P}\rangle = \int_{\Delta A}\langle P\rangle dA \quad (6)$$

The state of the system is known at the centre of the calculation cell and it is defined by the cell-averaged values $\langle\bar{u}_i\rangle$ and $\langle\bar{P}\rangle$. $t^{(n)}$ is the time level of the known variables while $t^{(n+1)}$ is the time level of the unknown variables. From the values of the fluid dynamic quantities at the time $t^{(n)}$ by means of the structural motion equations, the structural displacements are calculated and from the latter, the position of the cell vertices and the grid velocity $u_{g,i}^{(n)}$ are calculated. Given the values of $\langle\bar{u}_i\rangle^{(n)},\langle\bar{P}\rangle^{(n)},\langle\bar{k}\rangle^{(n)},\langle\bar{\omega}\rangle^{(n)}$ at the centre of the calculation cells at time $t^{(n)}$, the integration of the fluid motion equations (supplied with the turbulence closure relations for the Reynolds stress tensor) allows the calculation of $\langle\bar{u}_i\rangle^{(n+1)},\langle\bar{P}\rangle^{(n+1)}$ at time $t^{(n+1)}$.

The solution procedure for the fluid motion equations uses a five stage fourth order accurate Strong Stability Preserving Runge-Kutta (SSPRK) fractional-step method for the momentum equations and applies a pressure correction formulation to obtain a divergence free velocity field at each time level. Let, $\langle\bar{u}_i\rangle^{(n)}$ be the value of the i-th component of the fluid velocity at the time level n. The fluid velocity field $\langle\bar{u}_i\rangle^{(n+1)}$ at the time level n+1 is calculated through the following five stage iteration procedure. Let:

$$\langle\bar{u}_i\rangle^{(0)} = \langle\bar{u}_i\rangle^{(n)} \quad (7)$$

At each stage p (where, p = 1, 2, ..., 5) an auxiliary velocity field, $\langle\bar{u}_i\rangle^{*(p)}$ is obtained directly from momentum, Eq. 2 using values from the previous time level:

$$\langle\bar{u}_i\rangle^{*(p)} = \sum_{q=0}^{p-1}\left[\Omega_{pq}\langle\bar{u}_i\rangle^{(q)} + \Delta t\varphi_{pq}D\left[\langle u_i\rangle^{(q)}, t^{(n)} + d_q\Delta t\right]\right] \quad (8)$$

having indicated with $D[\langle u_i\rangle, t]$ the right-hand side of Eq. 2 divided for ΔA, in which the last term related to the pressure gradient has been omitted. Spiteri and Ruuth (2002) for the values of the coefficients Ω_{pq}, φ_{pq} and d_q. In general, the auxiliary velocity field of Eq. 8 will not satisfy the continuity equation. As a result, the velocity and the pressure fields are corrected in the following manner. By introducing a scalar potential ψ the well-known poisson pressure equation appears in the following integral form:

$$\int_L \frac{\partial\Psi^{(p)}}{\partial x_i} n_i dL = -\int_L \langle\bar{u}_i\rangle^{*(p)} n_i\, dL \quad (9)$$

where, L and n_i represent, respectively the contour of the calculation cell and the i-th component of the outward unit vector normal to the contour. The solution of Eq. 9

provides the calculation of the above-mentioned scalar potential ψ. The corrector velocity field $\langle \overline{u}_i \rangle^{c(p)}$ is calculated through the following relation:

$$\langle \overline{u}_i \rangle^{c(p)} = \frac{\partial \Psi^{(p)}}{\partial x_i} \tag{10}$$

The calculation of the velocity at stage p is given by:

$$\langle \overline{u}_i \rangle^{(p)} = \langle \overline{u}_i \rangle^{*(p)} + \langle \overline{u}_i \rangle^{c(p)} \tag{11}$$

The fluid velocity and pressure fields at the instant $t^{(n+1)}$ are respectively given by:

$$\langle \overline{u}_i \rangle^{(n+1)} = \langle \overline{u}_i \rangle^{(5)}, \ \langle \overline{P} \rangle^{(n+1)} = \frac{1}{\Delta t} \Psi^{(5)} \tag{12}$$

For the calculation of term D [⟨u_i⟩, t] the numerical approximations of integrals on the right-hand side of Eq. 2 is required. The aforementioned calculation is based on the following sequence:

High order WENO reconstructions from cell averaged values of the point values of the unknown variables at the centre of the contour segments which define the calculation cells. At the centre of the contour segment which is common with two adjacent cells, two point values of the unknown variables are reconstructed by means of two WENO reconstructions defined on two adjacent cells.

Advancing in time of the point values of the unknown variables at the centre of the contour segments by means of the so-called exact solution of the Riemann problem with initial data given by the pair of point values computed by two WENO reconstructions defined on the two adjacent cells. Calculation of the spatial integrals which define D [⟨u_i⟩, t].

For further details on the WENO reconstructions, the advancing in time of the unknown variables and on the calculation of the spatial integrals which define D [⟨u_i⟩, t], Gallerano and Cannata (2011b), Gallerano *et al.* (2012, 2014). The numerical integration of the turbulence closure relations allows the calculation of $\langle \overline{F} \rangle^{(n+1)}, \langle \overline{\varpi} \rangle^{(n+1)}$ and the Reynolds stress tensor at the time $t^{(n+1)}$ via. Eq. 3. Discretising Eq. 8 and 9 using the numerical method introduced above, entails the risk of introducing mass sources or sinks in the flow field if the velocity $u_{g,i}$ and the change volume over time are not treated consistently. For this reason, The Geometric Conservation Law (GCL):

$$\frac{d}{dt} \int_{\Delta A} dA + \int_{\Delta A} \frac{\partial u_{g,i}}{\partial x_i} dA = 0 \tag{13}$$

needs to be satisfied. To warrant consistency, Eq. 13 is used to determine the grid velocity by the given change of volume of the computational cell (Hertel *et al.*, 2013). In order to update the coordinates of the control volume vertices at all times, a mesh movement algorithm based on using inverse distance weighting (Uyttersprot, 2014) has been used in order to interpolate the displacements of the boundary nodes to the whole flow mesh.

RESULTS AND DISCUSSION

Details of the numerical simulation: The proposed simulation model is used in order to evaluate the aero-elastic stability of the Forth Road Bridge deck in its current configuration (configuration 1). Figuer 1 shows the geometric characteristics of the forth road bridge deck in its current configuration (configuration 1) are shown. Table 1 shows the values of the geometrical parameters (overall width and maximum depth) and the structural parameters (mass per unit length and mass moment of inertia per unit length, natural heaving frequency and natural torsional frequency, heaving and torsional damping ratios) of the Forth Road Bridge deck are listed.

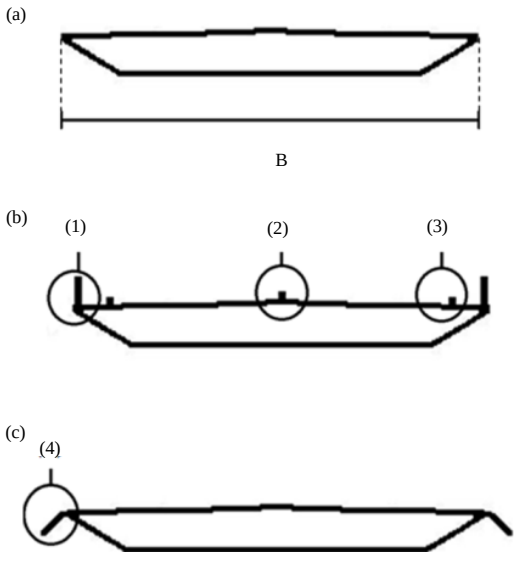

Fig. 1: Forth road bridge deck; a) Configuration 1-construction state configuration: B deck width; b) C onfiguration 2-configuration with cross-section details: 1 Vertical barriers; 2 Dividing strip; 3 Railings; c) Configuration 3-configuration modified through a couple of sloping barriers and 4 Sloping barriers

Table 1: Geometrical and structural parameters of the forth road bridge deck (Robertson *et al*., 2003)

Veriables	Values
Overall width	31.2 m
Maximum depth	3.2 m
Mass moment of inertia per unit length	2.13×10^6 (kgm^2/m)
Mass per unit length	17.3×10^3 (kg/m)
Torsional damping ratio	0.14%
Heaving damping ratio	0.31%
Natural torsional frequency	0.4 Hz
Natural heaving frequency	0.174 Hz

The flow domain considered for the bridge deck is 10B by 5B. At the upwind boundary of the computational domain a zero gradient boundary condition is imposed for the fluid pressure while a constant value is set for the other fluid quantities (velocity, turbulent kinetic energy and turbulence frequency). The Reynolds number used in every simulation derives from the undisturbed inflow wind velocity U, the actual kinematic viscosity ($v = 1.23\times10^{-5}$ m^2/sec) and the width B of the cross-section. In particular, the Reynolds number used for an undisturbed wind velocity U = 87.4 m/sec is about 1.95×10^8. At the solid walls the near-wall treatment proposed by Menter *et al*. (2003) is used which makes it possible to switch automatically from a classical low-Re formulation on fine grids to a wall function formulation on coarser meshes. At the outlet a constant pressure boundary condition is set while the zero gradient boundary condition is imposed for the other fluid dynamic quantities (fluid velocity, the turbulent kinetic energy and the turbulence frequency). In all the simulations a maximum Courant number of 1.0 is imposed which produces a minimum time step close to $\Delta t = 1\times10^{-5}$ s at $Re = 1.95\times10^8$.

The aerodynamic fields which develop around the Forth Road Bridge deck in its current configuration are simulated by using the wall-function. The simulations are performed on a grid made up of 275360 cells in which the cell size is varied gradually with a geometric progression of 1.02 in all directions. For an undisturbed wind velocity U = 87.4 m/sec, at the solid walls the average value of the non-dimensional height y^+ is close to 20 and the maximum value is close to 80.

Accuracy of the proposed model: Aiming to verify the spatial convergence of the numerical simulations, a grid convergence test is performed. In particular, similarly to that made by Haque *et al*. (2015), the grid convergence test proposed by Roache (1998) is carried out. This test which is based on the principle of Richardson extrapolation, requires three different grids: specifically, a fine grid (1), a medium grid (2) and a coarse grid (3). An estimate of the per cent error obtained with the fine grid (1) with respect to the converged solution is given by the grid convergence index GCI_{12}:

$$GCI_{12} = \frac{F_S\left|(\phi_1 - \phi_2)/\phi_2\right|}{r^P - 1} \quad (14)$$

Where:

ϕ and ϕ = The target parameters obtained, respectively by grid (1) and (2)
F_S = The safety factor
r = The adopted refinement factor
P = The observed order of convergence

A safety factor F_S= 1.25 is adopted and a constant refinement factor $r_{12} = r_{23} = r = 1.40$ is used where r_{12} is estimated as the ratio between the grid spacing of the fine grid and that of the medium grid and r_{23} is estimated as the ratio between the grid spacing of the medium grid and that of the coarse grid. The value of P is calculated by the relation (Roache, 1998):

$$P = \ln\left(\frac{\phi_3 - \phi_2}{\phi_2 - \phi_1}\right)/\ln(r) \quad (15)$$

where, ϕ_3 is the target parameter obtained from grid (3). In order to check that the solution obtained with the fine grid (1) reaches the asymptotic range of convergence (ARG), the following relation is used:

$$ARC = \frac{GCI_{23}}{r^P GCI_{12}} \quad (16)$$

where, GCI_{23} is calculated by replacing ϕ_1 with ϕ_2 and ϕ_2 with ϕ_3. If Eq. 16 yields a value of 1, this implies that the fine grid (1) reached the ARC.

The test is conducted in a static configuration (all the degrees of freedom of the cross-section are blocked) for an undisturbed wind velocity U = 87.4 m/sec. For every simulation performed the time histories of the drag and the lift forces and the aerodynamic moment are determined, together with those of the fluid velocity at two different points placed in the wake of the body. The time averaged and the root-mean-square values of the drag coefficient $C_D = F_D/(0.5\rho U^2 D)$, the lift coefficient $C_L = F_L/(0.5\rho U^2 B)$ and the moment coefficient $C_M = M/(0.5\rho U^2 B^2)$, together with the value of the Strouhal number $St = (f_S D)/U$, are taken as parameter of interest. F_D, F_L and M are respectively the drag force, the lift force and the aerodynamic moment exerted by the fluid on the structure, U the undisturbed wind velocity, D and B the depth and the width of the deck cross-section, ρ the fluid density. f_S is the shedding frequency and is computed from the time history of the fluid velocity at the two different points placed in the wake of the cylinder. In order to perform the above test,

Table 2: Grid convergence test for the forth road bridge deck

				Grid convergence test		
Target parameter	Coarse grid	Medium grid	Finest grid	GCI_{23} (%)	GCI_{12} (%)	ARC
Mean drag	0.6313	0.6413	0.6443	0.8353568	0.2494401	1.004678
RMS of drag	0.0082	0.0079	0.0078	2.3734177	0.8012821	0.9873418
Mean lift	-0.6632	-0.6801	-0.6851	1.3325739	0.397625	1.0074559
RMS of lift	0.2679	0.2877	0.2934	3.4776917	0.9817039	1.0198123
Mean moment	-0.4568	-0.4479	-0.4453	1.0250658	0.3012059	0.9941951
RMS of moment	0.0558	0.0576	0.0581	1.5024038	0.4137429	1.0086806
Strouhal number	0.253	0.253	0.253	0	0	1

three grids are used: a fine grid (described before) that is made up of 275360 calculation cells and hereafter is named GRID1 a medium grid, named GRID2 which is composed of cells a coarse grid, named GRID3 which is composed of 72448. For the latter grids, at the solid walls the average value of the non-dimensional height y^+ is respectively, 28 for GRID2 and 39 for GRID3 and the maximum value is respectively 111 and 144. The geometric progression is 1.03 for GRID2 and 1.04 for GRID3. These geometric progressions (as well as the grid spacings) are selected such that $r_{12} = r_{23} = 1.40$. Table 2 shows the time averaged and the root-mean-square values of the aerodynamic coefficients and the Strouhal number obtained by using the three different grids are reported, together with the results of the grid convergence test. By observing Table 2, it is possible to deduce that each grid level yields solutions which are in the asymptotic range of convergence for the computed solution and the fine grid has a maximum error >5%. In the following it is implied that the results are obtained by using GRID1, if otherwise not stated.

Stability analysis: The initial conditions in the stability analyses must be treated carefully. The instantaneous application of the full wind speed to an initially stationary structure leads to large transient initial motions from which it is difficult to extract definitive conclusions about the stability of small oscillations. To eliminate this problem, according to Frandsen (2004) for every simulation performed the structural damping values are set to near-critical values for the first ten seconds of the simulation until the structure settles into a near-stationary configuration after which the damping values are changed to their estimated full-scale values. During this transient phase, the stiffness constants of the vertical and torsional spring are gradually relaxed from magnified values to those calibrated to give the correct natural frequencies in the fundamental modes.

Figure 2 shows the time histories of the torsional displacements and the vertical displacements produced for an undisturbed wind velocity U =74.9 m/sec (U_θ = 6.0 where $U_\theta = U/(f_\theta B)$ is the reduced wind velocity and f_θ is the natural torsional vibration frequency of the cylinder)

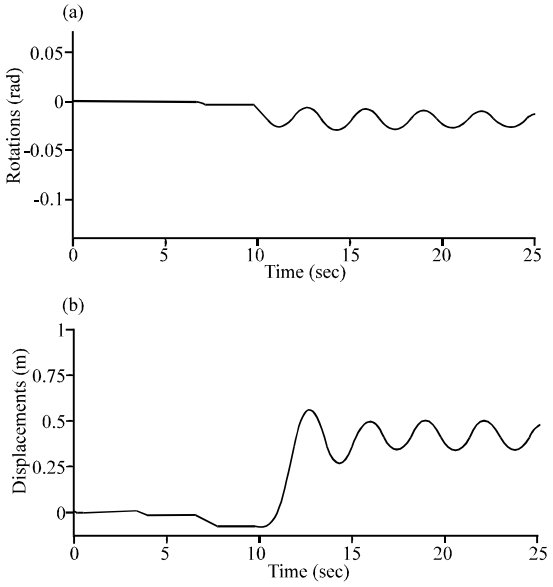

Fig. 2: Forth Road Bridge deck; a) Time history of the torsional displacements and b) Vertical displacements (configuration 1-U_θ = 6.0)

are shown. From the Fig. it can be seen that during the first seconds of the simulation (t<10 sec) in which the structure is gradually released, the gravity centre slightly drifts downward from the equilibrium position and the deck slightly rotates in a clockwise direction. In the instants immediately after t = 10 sec the structure continues to rotate clockwise so much, so that, the wind angle of attack exceeds the value for which the resultant of the aerodynamic forces and consequently, the vertical displacement of the gravity centre change direction (from downward to upward). From the figure itself it can be seen that the oscillatory motion produced after this transient phase shows a slow but constant decay of both the vertical and angular displacements: the value of the imposed wind velocity (U_θ = 6.0) lies under the critical flutter wind velocity value. Figure 3 shows the time histories of the rotations and the vertical displacements obtained for an undisturbed wind velocity U = 87.4 m/sec (U_θ = 7.0) are shown. In both cases, a constant growth of the displacements is observed: the value of the imposed

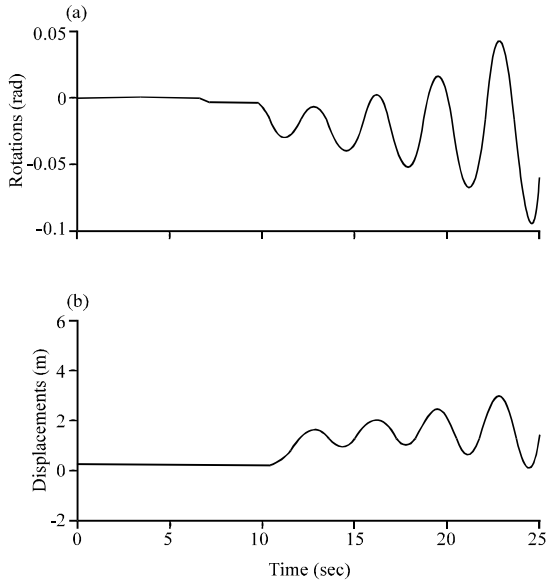

Fig. 3: Forth road bridge deck; a) Time history of the torsional displacements and b) Vertical displacements (configuration 1-U_θ = 7.0)

wind velocity (U_θ = 7.0) lies above the critical flutter wind velocity. From Fig. 2 and 3, it can be seen that the value of the mean rotation around which the instantaneous values of the rotation oscillate is not fixed but increases (in absolute value) going from the first to the second case. It follows that also the mean wind angle of attack increases (in absolute value) going from the first to the second case. Specifically, for U = 74.9 m/sec the instantaneous values of the wind angle of attack oscillate around a mean angle of attack roughly equal to -0.019 rad whilst for U = 87.4 m/sec the instantaneous values of the wind angle of attack oscillate around -0.027 rad. Consequently the aerostatic vertical displacement which is due to the aerostatic component of the wind load increases from about 0.4 m to about 1.5 m, i.e., more than linearly with the square of the wind velocity.

Validation of the proposed model: The numerical results are compared with those obtained from the wind tunnel tests described in the work by Robertson *et al.* (2003). Figure 4 shows the damping coefficient of the rotations versus the reduced wind velocity curve is plotted. The critical flutter wind velocity obtained is U^* = 79.1 m/sec ($U_\theta^* = 6.34$) in very good agreement with the experimental results reported by Robertson *et al.* (2003) ($U_\theta^* \approx 6.35$). For each of the considered reduced velocity, the frequencies of the rotational and vertical motion are calculated: it is found that for wind velocities equal to or greater than the critical flutter velocity these

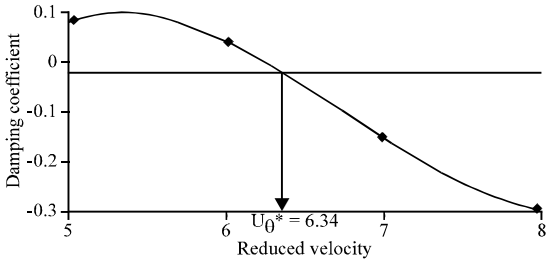

Fig. 4: Forth Road Bridge deck. Damping coefficient of the displacements vs. reduced velocity (configuration 1)

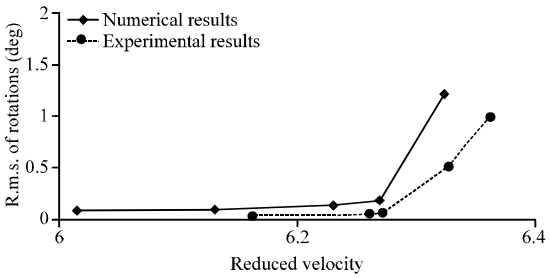

Fig. 5: Forth road bridge deck. Root mean square of torsional displacements vs. reduced velocity (configuration 1): numerical results (present work) and experimental results (Robertson *et al.*, 2003)

frequencies synchronize on a common frequency. This result is consistent with that shown in Robertson *et al.* (2003). Lastly, in Fig. 5 the root mean square values of rotational displacements are plotted against the reduced velocity values. In the latter figure, the values obtained numerically are shown together with those obtained in the wind tunnel tests reported by Robertson *et al.* (2003). From Fig. 5, it can be seen that the numerical results are in good agreement with the experimental ones.

Coupled flutter mechanism: In the following the onset mechanism of the aeroelastic instability is shown. The evolution of the aerodynamic fields and the structural motion for an undisturbed wind velocity U = 87.4 m/sec (U_θ = 7.0) is analysed during a structural oscillation cycle in which the oscillation amplitudes are still limited. Figure 6a shows the time histories of the infinitesimal vertical displacement of the gravity centre and the resultant of the forces (per unit area) normal to the deck surface exerted by the fluid on the structure (aerodynamic forces) are shown jointly. In Fig. 6 b the time histories of the infinitesimal angular displacement of the deck and the twisting moment generated by the same resultant are shown jointly. The cycle of structural oscillation shown in Fig. 6a, b corresponds to the time interval

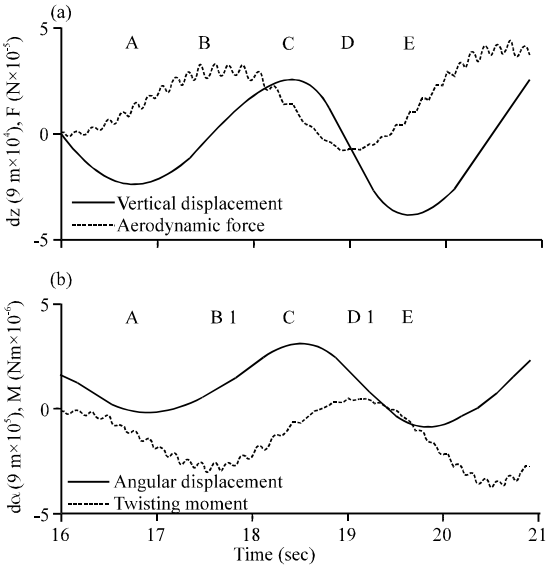

Fig. 6: Forth road bridge deck-configuration 1; a) Time histories of the infinitesimal vertical displacement of the gravity centre (solid line) and the resultant of the aerodynamic forces (dashed line) and b) Time histories of the infinitesimal angular displacement of the deck (solid line) and the twisting moment generated by the resultant (dashed line)

between two instants (indicated with the letters A and E in Fig 6 a, b when the infinitesimal vertical displacement of the downward moving gravity centre assumes a relative minimum value.

The examination of Fig. 6 stresses that during the time interval A-B and D-E of the above cycle the resultant of the aerodynamic forces acts in the opposite direction to the vertical velocity of the deck gravity centre, whilst in the time interval B-D the resultant acts in the same direction as the vertical velocity. The result of the integral of the research, defined as the product between the resultant and the infinitesimal displacement of the gravity centre of the deck, over the interval B-D is approximately equal to 261 kJ. This integral is much higher, in absolute value, than the sum of the integral calculated over A-B (approximately -97 kJ) and the integral calculated over D-E (approximately -59 kJ). The net energy contribution (approximately 104 kJ) of the resultant of the aerodynamic forces to the translational motion of the deck is that of making the same motion unstable. Similar considerations can be made regarding the twisting moment generated by the resultant of the aerodynamic forces.

Based on the analysis of the aerodynamic fields and the structural motion during the first cycles of oscillations of the deck (when the structure still exhibits oscillations of small amplitudes), it is then possible to deduce that the reason for the onset of the instability lies in the fact that there are some portions of the cycle within each of the first oscillation cycles in which the aerodynamic field provides both the translational and the rotational motion with a higher supply of energy than that subtracted from the deck motion in the rest of the cycle.

Once the two-degree-of-freedom instability has been triggered, a progressive increase of the maximum amplitudes of the rotation angle takes place. Once a threshold value of the above angle is exceeded the recirculation bubble which pulsates in proximity of the leading edge during the onset phase just described, starts to drift along the deck surface. From this point on the modalities of amplification of the oscillations have a different dynamic to the one described above. Figure 7a-g show the fluid velocity fields that develop around the deck in four instants within ½ cycle in which the amplitudes of the oscillations have reached high values. In Fig. 7b, d, f and h are shown the distributions of the forces per unit area normal to the deck surface exerted by the fluid on the structure (aerodynamic forces) in the same instants.

From the examination of Fig. 7, it results that the reason for the amplification of the instability lies in the formation and the drift of large vortical formations along the deck surface. From the simulation of the phenomenon it emerges that during the whole ½ cycle of structural oscillations (as previously defined), the sign of the twisting moment generated by the resultant of the components normal to the upper surface of the forces acting on the structure is always coherent with the sign of rotation. Consequently, there is a continuous supply of energy from the fluid dynamic field to the structure, that constitutes the reason for the amplification of the instability of the torsional motion.

Effect of the aerodynamic appendices: In this section, the effects of aerodynamic appendices on the flutter characteristics of the Forth road bridge are investigated via. the proposed simulation model. Two case studies are considered: in the first one (configuration), the impact of cross section details (vertical barriers, railings, dividing strip) is evaluated; in the second one (configuration), the efficacy of a couple of sloping barriers at the edges of the deck is assessed. Figure 1b, c show, respectively the geometrical features of the deck in its two variants. The dividing strip, the railings and the vertical barriers shown in Fig. 1b are respectively 2.0, 0.73 and 0.75 m high whilst the sloped barriers shown in Fig. 1c are inclined by 45 degrees to the vertical and are 2.0 m high. The simulations are performed on a grid made up respectively of 548020 cells for configuration 2 and 276520 for configuration 3.

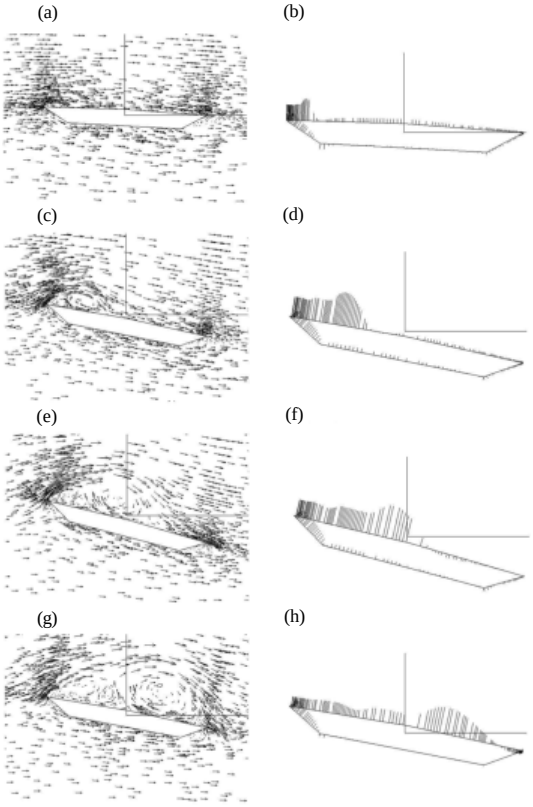

Fig. 7: Forth road bridge deck-configuration; a, c, e and g) Velocity fields of the fluid during the oscillation and b, d, f and h) Distributions of the aerodynamic forces during the oscillation

Firstly, the static behaviour of the basic configuration (configuration 1) and the two modified configurations is investigated. To this purpose, the calculation is performed of the static aerodynamic coefficients (lift, drag and moment coefficients) in all the three considered configurations. Table 3 reports the time-averaged values of the lift coefficient C_L, the drag coefficient C_D and the moment coefficient C_M computed for the three considered configurations at different Reynolds numbers ($1.39\times10^7<Re<1.95\times10^8$). This table reports, for each of the considered quantities, two different values: the first value is related to the lowest Reynolds number ($Re = 1.39\times10^7$), whilst the second value is related to the highest Reynolds number ($Re = 1.95\times10^8$). By examining Table 3, it is possible to deduce that, compared to configuration 1, the presence of the cross-section details (configuration 2) does not provoke relevant changes in the lift coefficient whilst, as a result of the substantial growth of the vertical area exposed to the incident wind, a significant increase in the drag coefficient is observed. With regard to configuration 3, it is possible to understand that the moment coefficient noticeably decreases as a result of the introduction of the sloping barriers whilst only slight variations are observed in the drag and the moment coefficients.

Table 3: Time averaged drag, lift and moment coefficients and strouhal number of the Forth Road Bridge deck

Veriables	Drag coefficient	Lift coefficient	Moment coefficient	Strouhal number
Configuration 1	0.578÷0.644	-0.584÷-0.685	-0.391÷-0.445	0.23÷0.25
Configuration 2	0.982÷1.134	-0.595÷-0.696	-0.452÷-0.628	0.22÷0.24
Configuration 3	0.379÷0.441	-1.951÷-2.444	-0.018÷-0.043	0.24÷0.27

Table 3 also reports the values of the Strouhal number St computed for the three configurations in the same range of Reynolds number ($1.39\times10^7<Re<1.95\times10^8$). The examination of Table 3 allows one to deduce that the Strouhal number slightly changes when passing from the basic configuration (configuration 1) to the two modified configurations. In particular, as a results of the introduction of the sloping barriers a slight increase is registered in the computed values of the Strouhal number, which range between 0.23 and 0.25 in configuration 1 and between 0.24 and 0.27 in configuration 3. Based on the Strouhal number, the critical velocity for which the Vortex Induced Vibration (VIV) instability takes place can be estimated by means of the expression $U^{VIV} = (\Omega_y D)/St$, being Ω_y the natural heaving frequency of the bridge deck. Hence, the critical wind VIV velocity is estimated to be slightly lower in configuration 3 (2.2 m/sec) than in configuration 1 (2.3 m/sec), from which it is concluded that the introduction of the sloping barriers slightly deteriorate the deck sensitivity to the VIV instability.

Lastly, the critical wind flutter velocity is identified for the three considered configurations. In configuration 2, this velocity is found to be $U^* = 78.5$ m/sec ($U^*_\infty = 6.29$), so slightly lower than in configuration 1. Therefore it can be deduced that the presence of the cross-section details has a negative impact on the aero-elastic stability of the deck. This can be explained by considering that due to the presence of the cross-section details, the flow detachment near the leading edge is magnified and consequently, the formation and drift of large vortices along the deck surface is facilitated. By contrast, in configuration 3 the critical wind flutter velocity value is found to be ($U^* = 82.6$ m/sec ($U^*_\infty = 6.62$)), so, slightly higher than in configuration 1. Compared to the basic configuration, a relevant decrease in the amplitudes of the wind-induced oscillations is registered. This is due to the fact that the presence of the sloping barriers reduces, compared to the basic configuration, the flow detachment at the leading edge, thus, delaying the formation and the drifting of large vortices along the deck surface. Consequently, this modification can be considered effective with regard to the flutter sensitivity of the deck.

CONCLUSION

In this research the effects produced by aerodynamic appendices on the aeroelastic stability of long-span bridge decks have been investigated. A simulation model has been presented by which the structural motion and the fluid flow are together and simultaneously simulated. The proposed finite volume method is based on high order Weighted Essentially Non-Oscillatory (WENO) reconstructions. The time discretisation is performed by a five stage fourth order accurate Strong Stability Preserving Runge-Kutta (SSPRK) method. It has been shown that the proposed numerical method makes it possible to ensure both high accuracy in time and space. The simulation model has been validated by comparing the numerical results with experimental data and has been applied to the evaluation of the aeroelastic stability of the forth road suspension bridge deck. The effects of aerodynamic appendices on the flutter characteristics of the Forth Road Bridge have been investigated via the proposed simulation model. It has been demonstrated that the presence of the cross-section details (barriers, railings, dividing strips) makes the aeroelastic stability of the deck worse and that the flutter sensitivity is mitigated by introducing a couple of sloping barriers at the edges of the deck.

REFERENCES

Astiz, M.A., 1998. Flutter stability of very long suspension bridges. J. Bridge Eng., 3: 132-139.

Braun, A.L. and A.M. Awruch, 2008. Finite element simulation of the wind action over bridge sectional models: Application to the Guama River Bridge (Pará State, Brazil). Finite Ele. Anal. Des., 44: 105-122.

Bruno, L. and S. Khris, 2003. The validity of 2D numerical simulations of vortical structures around a bridge deck. Math. Comput. Modell., 37: 795-828.

Cheng, Y., F.S. Lien, E. Yee and R. Sinclair, 2003. A comparison of large eddy simulations with a standard k-å Reynolds-averaged navier-stokes model for the prediction of a fully developed turbulent flow over a matrix of cubes. J. Wind Eng. Ind. Aerodyn., 91: 1301-1328.

Cioffi, F. and F. Gallerano, 2006. From rooted to floating vegetal species in lagoons as a consequence of the increases of external nutrient load: An analysis by model of the species selection mechanism. Appl. Math. Modell., 30: 10-37.

Dowell, E.H., 2014. A Modern Course in Aeroelasticity. Springer, Berlin, Germany, ISBN:978-3-319-09452-6, Pages: 697.

Frandsen, J.B., 2004. Numerical bridge deck studies using finite elements, Part I: Flutter. J. Fluids Struct., 19: 171-191.

Gallerano, F. and G. Cannata, 2011a. Central WENO scheme for the integral form of contravariant shallow-water equations. Intl. J. Numer. Methods Fluids, 67: 939-959.

Gallerano, F. and G. Cannata, 2011b. Compatibility of reservoir sediment flushing and river protection. J. Hydraul. Eng., 137: 1111-1125.

Gallerano, F., G. Cannata and F. Lasaponara, 2016b. A new numerical model for simulations of wave transformation, breaking and long-shore currents in complex coastal regions. Intl. J. Numer. Methods Fluids, 80: 571-613.

Gallerano, F., G. Cannata and F. Lasaponara, 2016a. Numerical simulation of wave transformation, breaking and runup by a contravariant fully non-linear Boussinesq equations model. J. Hydrodyn. Ser. B., 28: 379-388.

Gallerano, F., G. Cannata and M. Tamburrino, 2012. Upwind WENO scheme for shallow water equations in contravariant formulation. Comput. Fluids, 62: 1-12.

Gallerano, F., G. Cannata and M. Villani, 2014. An integral contravariant formulation of the fully non-linear Boussinesq equations. Coastal Eng., 83: 119-136.

Haan, F.L., 2000. The effects of turbulence on the aerodynamics of long-span bridges. Ph.D. Thesis, University of Notre Dame, Notre Dame, Indiana.

Haque, M.N., H. Katsuchi, H. Yamada and M. Nishio, 2016. Flow field analysis of a pentagonal-shaped bridge deck by unsteady RANS. Eng. Appl. Comput. Fluid Mech., 10: 1-16.

Hertel, C., M. Schumichen, S. Lobig, J. Frohlich and J. Lang, 2013. Adaptive large eddy simulation with moving grids. Theor. Comput. Fluid Dyn., 27: 817-841.

Larsen, A., 2000. Aerodynamics of the Tacoma Narrows bridge-60 years later. Struct. Eng. Intl., 10: 243-248.

Li, L., S.J. Sherwin and P.W. Bearman, 2002. A moving frame of reference algorithm for fluid/structure interaction of rotating and translating bodies. Intl. J. Numer. Methods Fluids, 38: 187-206.

Matsumoto, M., H. Matsumiya, S. Fujiwara and Y. Ito, 2010. New consideration on flutter properties based on step-by-step analysis. J. Wind Eng. Ind. Aerodyn., 98: 429-437.

Menter, F., J.C. Ferreira, T. Esch, B. Konno and A.C. Germany, 2003. The SST turbulence model with improved wall treatment for heat transfer predictions in gas turbines. Proceedings of the International Congress on Gas Turbine, November 2-7, 2003, Nippon Foundation, Tokyo, Japan, pp: 1-7.

Menter, F.R., 2009. Review of the shear-stress transport turbulence model experience from an industrial perspective. Intl. J. Computat. Fluid Dyn., 23: 305-316.

Miranda, S.D., L. Patruno, F. Ubertini and G. Vairo, 2014. On the identification of flutter derivatives of bridge decks via RANS turbulence models: Benchmarking on rectangular prisms. Eng. Struct., 76: 359-370.

Nieto, F., D.M. Hargreaves, J.S. Owen and S. Hernandez, 2015. On the applicability of 2D URANS and SST k-ù turbulence model to the fluid-structure interaction of rectangular cylinders. Eng. Appl. Computat. Fluid Mech., 9: 157-173.

Oka, S. and T. Ishihara, 2009. Numerical study of aerodynamic characteristics of a square prism in a uniform flow. J. Wind Eng. Ind. Aerodyn., 97: 548-559.

Roache, P.J., 1998. Verification of codes and calculations. AIAA. J., 36: 696-702.

Robertson, I., S.J. Sherwin and P.W. Bearman, 2003. Flutter instability prediction techniques for bridge deck sections. Intl. J. Numer. Methods Fluids, 43: 1239-1256.

Scanlan, R.H. and J.J. Tomko, 1971. Airfoil and bridge deck ?utter derivatives. J. Eng. Mech. Div. ASCE., 97: 1717-1737.

Spiteri, R.J. and S.J. Ruuth, 2002. A new class of optimal high-order strong-stability-preserving time discretization methods. SIAM. J. Numer. Anal., 40: 469-491.

Uyttersprot, L., 2014. Inverse distance weighting mesh deformation. MSc Thesis, Delft University of Technology, Delft, Netherlands.

Zhu, Z.W., M. Gu and Z.Q. Chen, 2007. Wind tunnel and CFD study on identification of flutter derivatives of a long-span self-anchored suspension bridge. Comput. Aided Civ. Infrastruct. Eng., 22: 541-554.